Article

Cancer Cell

MYC Drives Progression of Small Cell Lung Cancer to a Variant Neuroendocrine Subtype with Vulnerability to Aurora Kinase Inhibition

Graphical Abstract

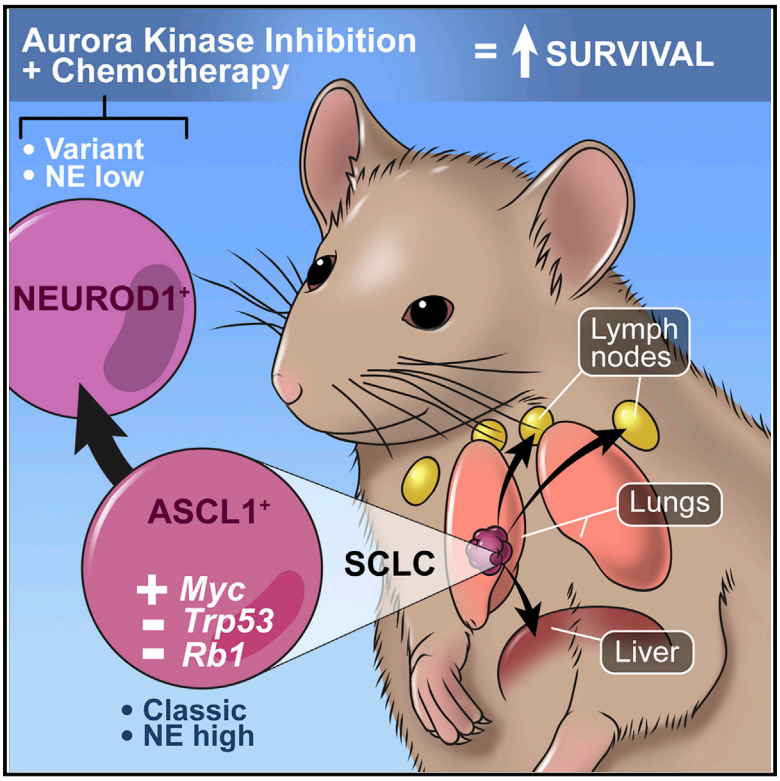

Authors

Gurkan Mollaoglu, Matthew R. Guthrie, Stefanie Böhm, ..., Robert J. Wechsler-Reya, Martin L. Sos, Trudy G. Oliver

Correspondence

martin.sos@uni-koeln.de (M.L.S.), trudy.oliver@hci.utah.edu (T.G.O.)

In Brief

Mollaoglu et al. generate a mouse model of small cell lung cancer (SCLC) with elevated *Myc* expression and loss of *Rb1* and *Trp53*. MYC promotes a neuroendocrine-low variant subtype of SCLC, which is paralleled in patients. Mouse and human SCLC with high MYC levels display sensitivity to Aurora kinase inhibition.

Highlights

- MYC dramatically accelerates tumorigenesis and metastases in *Rb1/Trp53* null SCLC
- MYC promotes a NEUROD1^{+}, neuroendocrine-low subtype with variant histopathology
- MYC-driven SCLCs are chemo-sensitive but rapidly relapse
- MYC sensitizes SCLC to combined Aurora kinase inhibition and chemotherapy treatment

Accession Numbers

GSE89660
GSE87034

Mollaoglu et al., 2017, Cancer Cell *31*, 270–285
February 13, 2017
http://dx.doi.org/10.1016/j.ccell.2016.12.005

CellPress

Cancer Cell
Article

MYC Drives Progression of Small Cell Lung Cancer to a Variant Neuroendocrine Subtype with Vulnerability to Aurora Kinase Inhibition

Gurkan Mollaoglu,[1,12] Matthew R. Guthrie,[1,12] Stefanie Böhm,[2,3,12] Johannes Brägelmann,[2,3,12] Ismail Can,[1] Paul M. Ballieu,[1] Annika Marx,[2,3] Julie George,[3] Christine Heinen,[3] Milind D. Chalishazar,[1] Haixia Cheng,[1] Abbie S. Ireland,[1] Kendall E. Denning,[1] Anandaroop Mukhopadhyay,[1] Jeffery M. Vahrenkamp,[1] Kristofer C. Berrett,[1] Timothy L. Mosbruger,[4] Jun Wang,[5] Jessica L. Kohan,[6] Mohamed E. Salama,[6] Benjamin L. Witt,[6] Martin Peifer,[3,7] Roman K. Thomas,[3,8,9] Jason Gertz,[1] Jane E. Johnson,[10] Adi F. Gazdar,[11] Robert J. Wechsler-Reya,[5] Martin L. Sos,[2,3,*] and Trudy G. Oliver[1,13,*]

[1]Department of Oncological Sciences, University of Utah, Huntsman Cancer Institute, Salt Lake City, UT 84112, USA
[2]Molecular Pathology, Institute for Pathology, Medical Faculty, University of Cologne, 50937 Cologne, Germany
[3]Department of Translational Genomics, Center of Integrated Oncology Cologne–Bonn, Medical Faculty, University of Cologne, 50931 Cologne, Germany
[4]Huntsman Cancer Institute, Bioinformatics Shared Resource, Salt Lake City, UT 84112, USA
[5]Tumor Initiation and Maintenance Program, Sanford Burnham Prebys Medical Discovery Institute, La Jolla, CA 92037, USA
[6]Department of Pathology, University of Utah and ARUP Laboratories, Salt Lake City, UT 84112, USA
[7]Center for Molecular Medicine Cologne, University of Cologne, 50931 Cologne, Germany
[8]Department of Pathology, University Hospital Cologne, 50937 Cologne, Germany
[9]German Cancer Research Center (DKFZ), German Cancer Consortium (DKTK), 69120 Heidelberg, Germany
[10]Department of Neuroscience, University of Texas Southwestern Medical Center, Dallas, TX 75390, USA
[11]Department of Pathology, Hamon Center for Therapeutic Oncology Research, UT Southwestern Medical Center, Dallas, TX 75235, USA
[12]Co-first author
[13]Lead Contact
*Correspondence: martin.sos@uni-koeln.de (M.L.S.), trudy.oliver@hci.utah.edu (T.G.O.)
http://dx.doi.org/10.1016/j.ccell.2016.12.005

SUMMARY

Loss of the tumor suppressors *RB1* and *TP53* and *MYC* amplification are frequent oncogenic events in small cell lung cancer (SCLC). We show that *Myc* expression cooperates with *Rb1* and *Trp53* loss in the mouse lung to promote aggressive, highly metastatic tumors, that are initially sensitive to chemotherapy followed by relapse, similar to human SCLC. Importantly, MYC drives a neuroendocrine-low "variant" subset of SCLC with high NEUROD1 expression corresponding to transcriptional profiles of human SCLC. Targeted drug screening reveals that SCLC with high *MYC* expression is vulnerable to Aurora kinase inhibition, which, combined with chemotherapy, strongly suppresses tumor progression and increases survival. These data identify molecular features for patient stratification and uncover a potential targeted treatment approach for MYC-driven SCLC.

INTRODUCTION

Small cell lung cancer (SCLC) comprises ~14% of all lung cancers and leads to ~30,000 deaths each year in the United States. The average survival time for patients with SCLC is ~10 months, with a 2-year survival rate of only 6% (Kalemkerian et al., 2013; Pietanza et al., 2015). The standard systemic therapy for SCLC is platinum-based chemotherapy with etoposide, which has

Significance

SCLC has historically been treated therapeutically as a homogeneous disease without molecular stratification. SCLC has a dismal prognosis with no targeted therapies approved for treatment. Tumors uniformly lack *RB1* and *TP53* and frequently acquire genomic amplifications of a *MYC* family member including *MYC*, *MYCL,* or *MYCN*. We developed an MYC-driven GEMM that recapitulates key features of human SCLC. Surprisingly, this model mimics a human SCLC subtype characterized by "variant" morphology, high *NEUROD1*, and low expression of neuroendocrine genes including *ASCL1*. Targeted drug screening revealed that MYC-driven SCLC is uniquely sensitive to Aurora kinase inhibitors, which dramatically improves chemotherapy response in vivo. Aurora kinase inhibition with first-line chemotherapy is a potential therapeutic approach for MYC-driven SCLC.

not changed for nearly 40 years. While 60%–80% of patients respond to chemotherapy, tumors rapidly develop resistance with cross-resistance to multiple therapies. SCLC is also highly metastatic with 50%–80% of patients harboring metastases at the time of autopsy (Elliott et al., 1987). These dismal statistics highlight the urgent need for a greater understanding of the disease and for new therapeutic approaches (Bunn et al., 2016).

Comprehensive genomic analyses of SCLC have reported loss-of-function alterations in *RB1* and *TP53* in 90%–100% of SCLCs (George et al., 2015; Peifer et al., 2012; Rudin et al., 2012). Amplification of *MYC* family genes including *MYC, MYCL,* and *MYCN*, also occur in ~20% of tumors and are mutually exclusive (Peifer et al., 2012; Sos et al., 2012). Genomic amplifications in *MYC* have been identified in 6%–25% of primary human tumors (Gazzeri et al., 1991; George et al., 2015) and in 30%–50% of SCLC cell lines (Johnson et al., 1992; Sos et al., 2012). *MYC* amplification has been associated with poor outcome, tumor progression, and treatment resistance, but how MYC impacts these processes has yet to be tested in vivo (Brennan et al., 1991; Johnson et al., 1987; Sos et al., 2012).

Human SCLC cell lines have been characterized as classic or variant, with variant lines exhibiting faster doubling times, frequent *MYC* amplification, reduced neuroendocrine marker expression, and loosely aggregated morphology (Carney et al., 1985; Gazdar et al., 1985; Johnson et al., 1992, 1996). Patients whose cell lines harbor *MYC* amplifications demonstrate poor survival compared with those without (Brennan et al., 1991; Johnson et al., 1987). The relationship of cell line morphology to human tumors and the factors that drive these phenotypes are not well understood; this is partly because biopsies from SCLC are small, infrequent, and often derived from chemo-naive patients. The classification of SCLC includes mixed or "combined" forms of SCLC (Travis et al., 2015), and it has been observed that ~10%–20% of SCLCs may lack expression of diagnostic neuroendocrine markers (George et al., 2015; Rekhtman, 2010; Travis, 2009), but these phenotypes currently do not impact therapeutic decisions.

Molecular signatures of tumor heterogeneity in SCLC have been discovered at the level of gene expression and methylation patterns, including an inverse relationship between the neurogenic transcription factors, Achaete-Scute Homologue 1 (ASCL1) and Neuronal Differentiation 1 (NEUROD1) (Borromeo et al., 2016; Poirier et al., 2013, 2015). ASCL1, but not NEUROD1, is required for tumorigenesis in a mouse model of classic SCLC indicating that ASCL1 is a key driver of at least this subset of tumors (Borromeo et al., 2016). In contrast, *NEUROD1*^{high} signatures are associated with variant morphology and *MYC* amplifications in human cell lines (Borromeo et al., 2016; Poirier et al., 2013). Mouse models, however, have not yielded variant, NEUROD1^{+} tumors, which has cast doubt on the physiological relevance of this molecular subset (Borromeo et al., 2016; Bunn et al., 2016).

Genetically engineered mouse models (GEMMs) of SCLC are based on simultaneous loss of *Rb1* and *Trp53* in the mouse lung. Mice develop SCLC with long latency (i.e., 10–15 months) and tumors frequently harbor *Mycl* amplifications similar to human SCLC (Calbo et al., 2011; Dooley et al., 2011; Meuwissen et al., 2003). *Mycl* overexpression in *Rb1*$^{fl/fl}$;*Trp53*$^{fl/fl}$ mice using a chimeric model accelerates lung tumor formation, demonstrating that *Mycl* is an SCLC driver (Huijbers et al., 2014; Semenova et al., 2015). In cooperation with *Rb1* and *Trp53* loss, deletion of the *Rb1* family member *Rbl2* (p130) or the *Pten* tumor suppressor shortens tumor latency but mice also develop variable histological subtypes (Cui et al., 2014; Gazdar et al., 2015; McFadden et al., 2014; Schaffer et al., 2010). Tumors from these GEMMs have been classified histopathologically as classic SCLC, large-cell neuroendocrine carcinoma (LCNEC), or non-small-cell lung cancer with neuroendocrine features (NSCLC-NE), but to date none have demonstrated variant SCLC pathology (Bunn et al., 2016; Gazdar et al., 2015). Here we describe a new GEMM of SCLC and use integrated genomic and transcriptomic analyses of human and murine SCLC to determine the impact of MYC on key clinical features of SCLC tumorigenesis and therapeutic response in vivo.

RESULTS

MYC Promotes Rapid SCLC in Cooperation with *Rb1* and *Trp53* Loss

We generated knockin Lox-Stop-Lox (LSL)-*Myc*^{T58A}-IRES-Luciferase mice that carry a Cre recombinase regulatable *Myc*^{T58A} allele in the *H11* locus (Figure S1A). These mice were crossed to *Rb1*$^{fl/fl}$*Trp53*$^{fl/fl}$ (RP) animals to generate *Rb1*$^{fl/fl}$*Trp53*$^{fl/fl}$*Myc*$^{LSL/LSL}$ (RPM) mice. Mice were infected intratracheally with adenoviruses carrying *Cre* driven by a neuroendocrine calcitonin gene-related peptide (*Cgrp*) promoter. CGRP-expressing cells have been demonstrated to be the predominant cell of origin in the RP model of SCLC (Sutherland et al., 2011). As a comparison, we infected *Rb1*$^{fl/fl}$*Trp53*$^{fl/fl}$*Pten*$^{fl/fl}$ (RPP) animals with Cgrp-Cre viruses, which develop SCLC within 5–8 months (Cui et al., 2014; Gazdar et al., 2015; McFadden et al., 2014). Within 5 weeks of viral infection, some RPM mice began to exhibit labored breathing, and had to be killed. RPM mice had significantly increased mortality compared with RPP mice (median survival of 60 versus 164 days, respectively) (Figure 1A). Compared with RPM mice, heterozygous *Rb1*$^{fl/fl}$*Trp53*$^{fl/fl}$*Myc*$^{LSL/+}$ (RPM$^{LSL/+}$) mice had a slightly longer median survival of 81 days (Figure S1B). As the RPM mice carry a luciferase allele, we monitored animals using bioluminescent imaging and the majority (n = 8 of 11) exhibited a signal in the chest area (Figure 1B). Upon killing, lungs were dissected and large tumors were found in the upper central airway, usually involving the main bronchi (Figure 1C).

We imaged a separate cohort of RPM mice between 5 and 7 weeks post-Cgrp-Cre infection using micro-computed tomography (microCT) imaging. In contrast to adenocarcinomas that develop in the distal and peripheral lung (Jackson et al., 2001; Oliver et al., 2010), RPM tumors were centrally located, exhibiting a donut-like pattern of density at major bronchi and large bronchioles (Figures 1D and 1E). To visualize tumors at earlier stages of development, we killed a cohort of mice at 1–4 weeks post-infection (Figures 1F and S1C–S1F). Small proliferating (Ki67^{+}) lesions were evident in or around the airways as early as 2–3 weeks (Figure S1F). By 5–6 weeks post-infection, tumors exhibited massive lymphatic invasion and perivascular and peribronchial spread (Figure 1G). Three board-certified pathologists classified all tumors as SCLC. While the overall appearances were consistent with human SCLC, tumors contained two populations of cells with distinct morphologies. One population

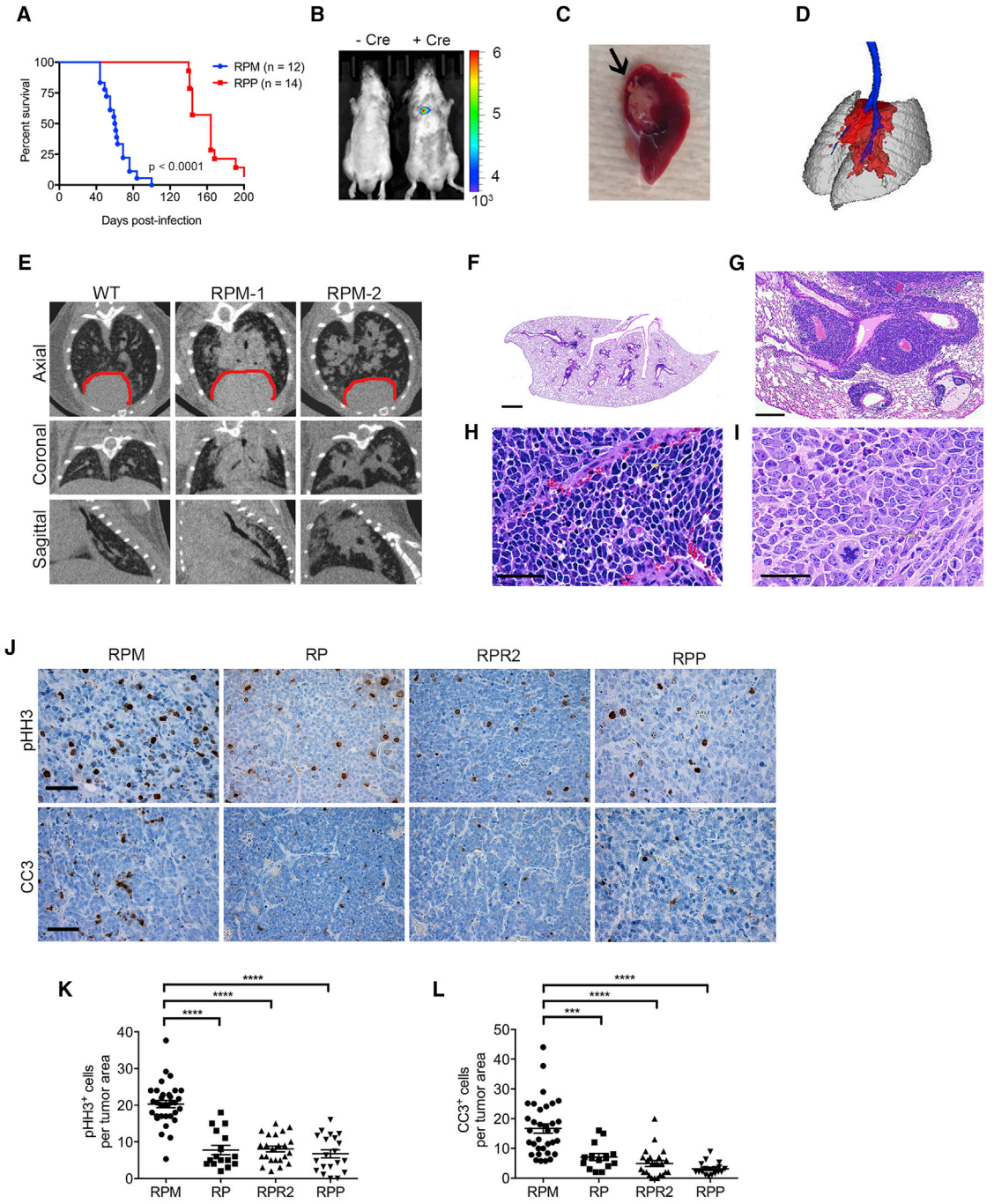

Figure 1. MYC Promotes Rapid SCLC in Cooperation with *Rb1* and *Trp53* Loss

(A) Survival of mice infected with 10^8 plaque-forming units (pfu) of Cgrp-Cre. Log rank (Mantel-Cox) test indicated.

(B) Representative bioluminescent imaging of uninfected (−Cre) or Cgrp-Cre- infected (+Cre) RPM mice at 69 days post-infection with 10^6 pfu virus. Units represent relative light units.

(C) Brightfield image of dissected lung from an RPM mouse with a tumor in the airway (indicated by black arrow) at 8 weeks post-infection.

(D) Three-dimensional rendering of microCT data with lungs in gray, tumor in red, and major airways in blue.

(E) MicroCT images in indicated planes from wild-type (WT) or RPM mice at 39 (RPM-1) and 44 (RPM-2) days post-infection with 10^8 pfu Cgrp-Cre. The red line surrounds the heart.

(F–I) Representative RPM lung H&E images: sections derived from 3 weeks post-infection (F); Scale bar, 1 mm. 7 weeks post-infection with perivascular and perilymphatic spread (G); Scale bar, 250 μm. Classic morphology (H) and variant morphology (I); Scale bars, 50 μm.

(J–L) IHC (J) and manual quantification of pHH3 (K), or CC3 (L) in indicated tumor models. Scale bars, 50 μm.

Error bars indicate mean ± SEM. Two-tailed unpaired t tests, ****p < 0.0001, ***p = 0.001. See also Figure S1.

had the features of typical "classic" SCLC, with small cells, scant ill-defined cytoplasm, finely granular nuclear chromatin, and inconspicuous nucleoli (Travis, 2012) (Figure 1H). The other population consisted of slightly larger cells with single, centrally located prominent nucleoli and well-defined eosinophilic cytoplasm, similar to what has been described as the variant form of SCLC (Gazdar et al., 1985) (Figure 1I). Individual tumors consisted of one of these forms or a mixture of both. A recent review on the pathology of murine neuroendocrine lung cancers failed to identify the variant form in these GEMMs (Gazdar et al., 2015). Of interest, LCNEC or NSCLC tumor components were not noted in RPM animals, although they have been described in other GEMMs (Gazdar et al., 2015).

Because human SCLC is highly proliferative and apoptotic (Travis, 2012), we examined cell proliferation and apoptosis in RPM tumors at 6–8 weeks post-infection. RPM tumors had significantly higher levels of proliferation as measured by phospho-histone H3 (pHH3) levels compared with RP, *Rb1*$^{fl/fl}$*Trp53*$^{fl/fl}$*Rbl2*$^{fl/fl}$ (RPR2) and RPP tumors (Figures 1J and 1K). RPM tumors exhibited areas of cell death, but we did not observe the Azzopardi phenomenon as noted in other GEMMs (Gazdar et al., 2015). RPM tumors exhibited significantly more apoptotic cells than other SCLC models as measured by immunohistochemistry (IHC) for cleaved caspase-3 (CC3) (Figures 1J and 1L). Compared with homozygous RPM tumors, RPM$^{LSL/+}$ tumors displayed subtly reduced levels of MYC (Figures S1G and S1H) but did not have statistically different levels of pHH3 or CC3 (Figures S1I and S1J). RPM tumors were uniformly negative for alveolar (i.e., SFTPC/SPC) and club cell (i.e., SCGB1A1/CCSP) markers (Figures S1K–S1M). NKX2-1, also known as TTF1, is expressed in the vast majority of adenocarcinomas and SCLCs and RPM, RPP, and LSL-*Kras*$^{G12D/+}$;*p53*$^{fl/fl}$ (KP) tumors expressed nuclear NKX2-1 as expected (Figures S1K and S1N). These data demonstrate that MYC dramatically accelerates tumor formation predominantly exhibiting variant histopathology.

MYC Promotes Neuroendocrine-Low SCLC with NEUROD1 Expression

Neuroendocrine differentiation is considered a hallmark of classic SCLC. Previous GEMMs recapitulate the classic phenotype and are frequently associated with *Mycl* amplifications (Calbo et al., 2011). In contrast, variant SCLC was previously reported to express low levels of neuroendocrine markers (Carney et al., 1985). Interestingly, RPM tumors recapitulate variant SCLC morphology and lack *Mycl* amplifications (Figure S2A). RPM tumors expressed significantly less *Mycl* and more *Myc* than tumors from RPP and RPR2 models (Figure S2B).

To determine whether *Myc* is associated with attenuation of neuroendocrine differentiation in vivo, we performed hierarchical clustering analyses of neuroendocrine markers that overlapped between published microarray data derived from RP (n = 10) and RPR2 tumors (n = 3) (Schaffer et al., 2010), as well as RNA sequencing (RNA-seq) data that we generated for additional RPR2 (n = 4) and RPM tumors (n = 11) (Figure 2A and Table S1). RPM tumors clustered independently from RP and RPR2 tumors and exhibited lower expression of the majority of neuroendocrine genes. Interestingly, RPM tumors had significantly reduced expression of the neurogenic transcription factor *Ascl1* but high expression of *Neurod1* (Figure 2B). Previous studies described distinct tumorigenic functions of ASCL1 and NEUROD1 in SCLC (Borromeo et al., 2016; Poirier et al., 2013, 2015), and we sought to further explore the association between high *Myc* expression and neuroendocrine differentiation in our model. First, we analyzed our mouse tumor RNA-seq data using gene set enrichment analysis (GSEA). We found that an *ASCL1*^{high} signature derived from gene expression profiling and chromatin immunoprecipitation sequencing (ChIP-seq) in human SCLC (Borromeo et al., 2016) was significantly depleted and a *NEUROD1*^{high} signature was significantly enriched in RPM compared with RPR2 tumors (Figure 2C). Next, we examined protein expression of ASCL1 and NEUROD1 in multiple GEMMs by IHC. All SCLC models harbored ASCL1^{+} lung tumors, but the levels of ASCL1 were significantly lower in RPM tumors compared with RP, RPR2, and RPP models (Figure 2D). In contrast, RPM tumors demonstrated high and heterogeneous expression of NEUROD1 compared with classic GEMMs, which was only rarely detected in RPP tumors (Figure 2D). Compared with homozygous RPM tumors, RPM$^{LSL/+}$ tumors had a trend toward higher ASCL1 and lower NEUROD1 expression but this was not statistically significant (Figure S2C). We also validated that RPM tumors express NEUROD1 by immunoblot using two independent antibodies, including the antibody used for IHC (Figure 2E). Together this suggests that MYC promotes a variant, neuroendocrine-low, NEUROD1^{+} subset of SCLC.

RPM Tumors Recapitulate a Molecular Subset of *MYC*-High Human SCLC

Next, we asked whether a connection between *MYC* expression and these two key regulators of neuroendocrine signaling is recapitulated in human SCLC (Borromeo et al., 2016; Poirier et al., 2013). We collected publicly available transcriptome sequencing data of 81 SCLC specimens (George et al., 2015) and 20 SCLC cell lines (Peifer et al., 2012; Rudin et al., 2012) and performed RNA-seq analysis on 14 additional SCLC cell lines. Hierarchical clustering analysis based on a predefined set of neuroendocrine markers (Table S1) led to robust separation of samples into groups with either low (group a) or high (groups b and c) *MYC* expression (Figure 3A). We observed distinct expression patterns of *NEUROD1* and *ASCL1* in these three groups, which distinguish classic and variant SCLC histology in cell lines and patient-derived xenograft (PDX) models (Poirier et al., 2013, 2015). Similar to RP and RPP tumors with low *Myc* expression (Figure 2B), we observed high expression of *ASCL1* in group a, but low expression of *ASCL1* in groups b and c, which were enriched with samples expressing high *MYC* levels (Figure 3B). In contrast, high *NEUROD1* expression was primarily present in group c enriched for high *MYC*-expressing samples (Figure 3A), resembling the expression profile of RPM tumors (Figure 2B). Moreover, GSEA of human patient samples stratified by *MYC* expression showed a significant enrichment of the *ASCL1*^{high} signature in *MYC*-low samples and enrichment of the *NEUROD1*^{high} signature in *MYC*-high samples (Figure 3C). We observed a very similar clustering pattern of samples with high *MYC* expression in a recently published collection of 65 SCLC cell lines (25 shared with our cell lines) that were analyzed using gene expression arrays (Figures S3A and S3B) (Polley et al., 2016). Thus, our data show that, in

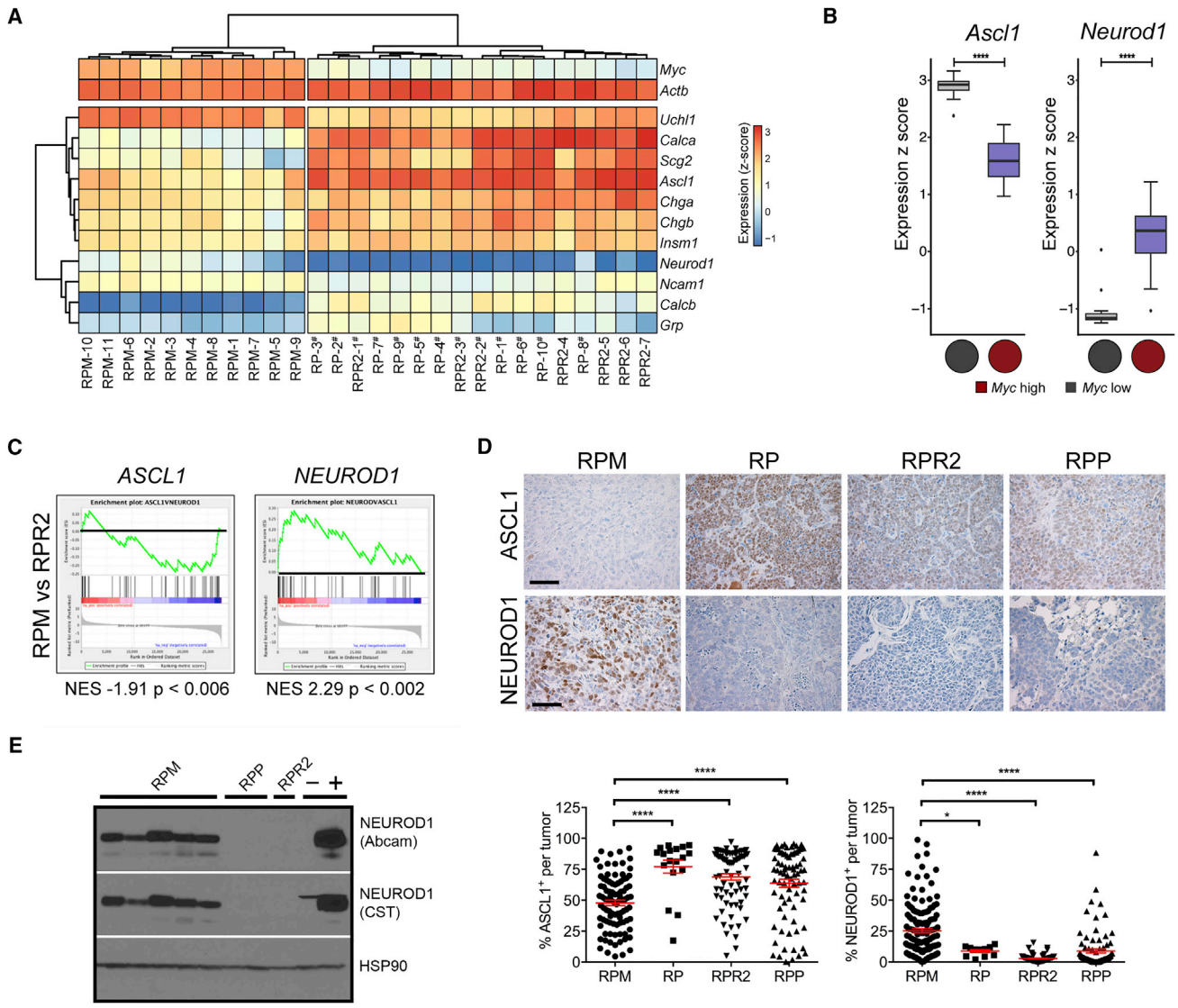

Figure 2. MYC Promotes Neuroendocrine-Low SCLC with NEUROD1 Expression In Vivo

(A) Hierarchical cluster analysis of NE markers from mouse tumors by expression array (indicated by #) or RNA-seq.

(B) Expression of *Ascl1* and *Neurod1* in mouse lung tumors. Proportions of *Myc*-high samples are indicated by pie charts.

(C) GSEA analysis from RPM versus RPR2 tumors with normalized enrichment scores (NES) and p values for *NEUROD1*^{high} and *ASCL1*^{high} signatures.

(D) IHC and automated quantification for ASCL1 and NEUROD1 in the indicated models. Scale bars, 50 μm.

(E) Immunoblot of mouse lung tumor lysates with NEUROD1 antibodies from the indicated source; HSP90 is loading control. Control human SCLC cell lines are H1963 (–) and H82 (+).

Error bars indicate mean ± SEM. Two-tailed unpaired t tests, ****p < 0.0001, *p < 0.01. See also Figure S2 and Table S1.

RPM mouse tumors, MYC is associated with differential expression of *Ascl1* and *Neurod1*, and that these expression profiles are highly conserved in human SCLC.

Given the greater variability of *ASCL1* and *NEUROD1* expression in human tumors compared with murine tumors by RNA-seq analysis, we went back to the RPM mouse model and examined the expression of ASCL1 and NEUROD1 at early (in situ) and late (invasive) time points. We found that in situ lesions from RPM animals 1–4 weeks post-infection were predominantly classic morphology with high ASCL1 expression (Figure 3D). Of 26 in situ lesions examined, 23 (88%) were clearly ASCL1^{+} while none were NEUROD1^{+}. In contrast, 44% of large invasive lesions at 6–8 weeks post-infection (18 of 41) exhibited variant morphology with NEUROD1 expression and either some or no ASCL1 expression. In addition, 17% of invasive tumors were low or negative for both ASCL1 and NEUROD1 (Figure 3D), similar to the subset of human tumors (group b) with the highest levels of *MYC* (Figure 3B). Some invasive tumors exhibited high levels of both ASCL1 and NEUROD1, although whether cells are intermixed or co-expressing both proteins cannot be determined by this method. RPM tumors also expressed other neuroendocrine markers including CGRP and neural cell adhesion

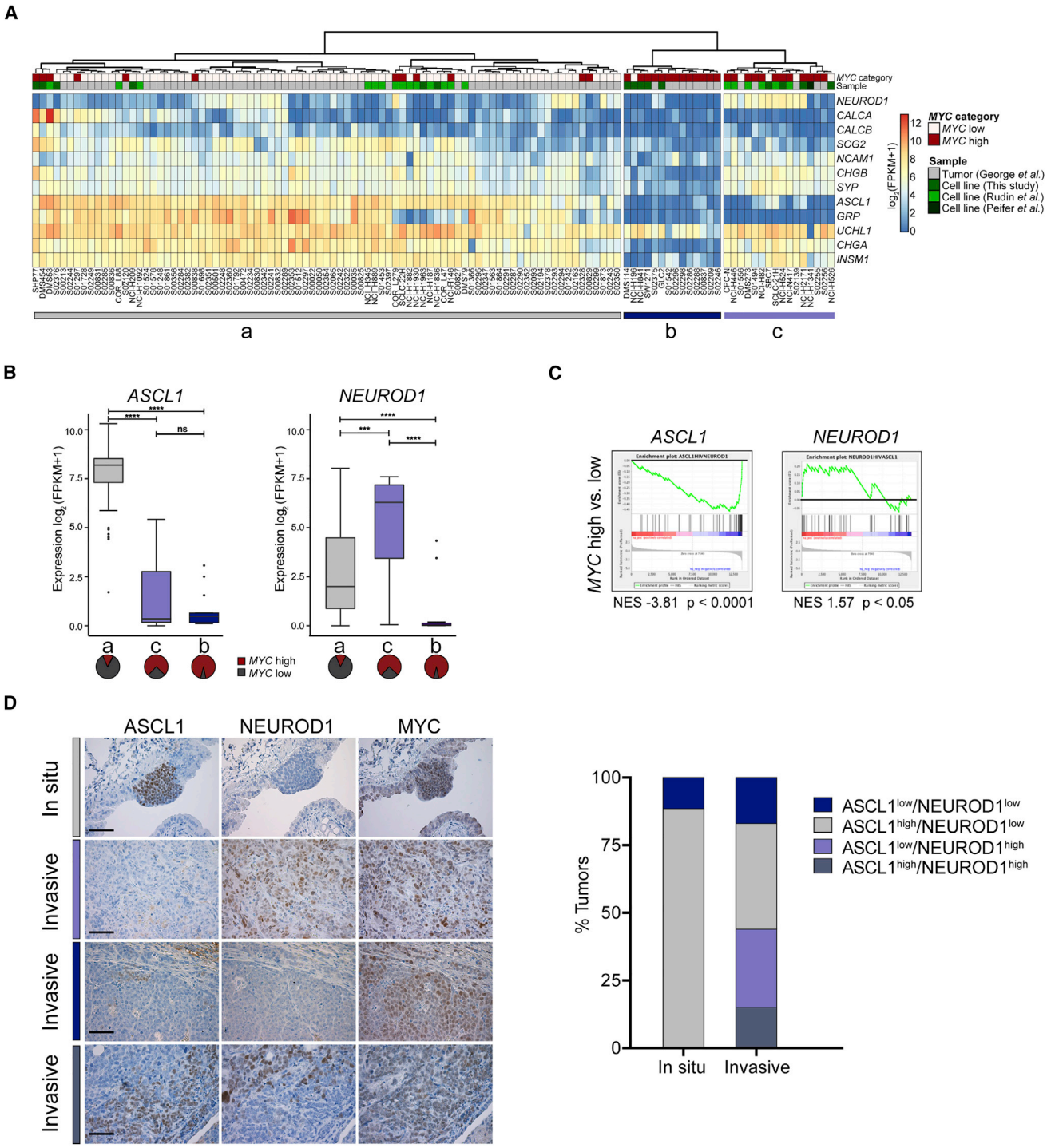

Figure 3. RPM Tumors Recapitulate a Molecular Subset of *MYC*-High Human SCLC

(A) Unsupervised hierarchical cluster analysis of NE markers from human SCLC patient samples and cell lines by RNA-seq. *MYC* expression, type of sample, and origin of dataset indicated above the heatmap.

(B) Expression of *ASCL1* and *NEUROD1* in human SCLCs and cell lines, grouped by NE marker expression according to (A). Proportions of *MYC*-high versus *MYC*-low samples are indicated by pie charts. Two-tailed unpaired t tests, ****p < 0.0001, ***p < 0.001. ns, not significant.

(C) GSEA analysis from *MYC*-high or *MYC*-low human SCLC with NES and p values for *NEUROD1*^{high} and *ASCL1*^{high} signatures.

(D) IHC serial sections from RPM lung tumor samples from in situ and invasive lesions stained with indicated antibodies (left). Tumors were grouped based on automated quantification of IHC staining as high or low for ASCL1 or NEUROD1. Proportions of tumors with each pattern (n = 26 in situ lesions; n = 41 invasive lesions) are indicated (right). Scale bars, 50 μm.

See also Figure S3.

molecule 1, which was evident in classic lesions and reduced in the majority of variant tumors, similar to ASCL1 expression (Figure S3C). Of note, RPM tumors exhibited robust staining for UCHL1 (also called PGP9.5) (Figure S3D), which was consistently expressed across murine and human SCLC tumors and cell lines irrespective of *MYC* status (Figures 2A and 3A). Overexpression of MYC in an RP cell line led to repression of synaptophysin (SYP) (Figure S3E), while knock down of MYC in *MYC*-amplified SCLC cell lines led to an increase in SYP mRNA and protein (Figures S3F and S3G), suggesting that MYC may indeed be involved in the modulation of neuroendocrine differentiation. While *MYC* has been described as a target gene of NEUROD1 (Borromeo et al., 2016), we did not identify *Neurod1* as an MYC target gene in RPM cell lines analyzed by ChIP-seq (Figure S3H). Given that MYC is expressed in in situ lesions in the absence of NEUROD1 expression (Figure 3D), this suggests that MYC's role in NEUROD1 regulation is likely through indirect mechanisms. Together, this indicates that high MYC expression during tumor progression modulates the neuroendocrine phenotype of SCLC and can lead to advanced lesions with heterogeneous patterns of neuroendocrine differentiation.

MYC-Driven Tumors Are Highly Metastatic Similar to the Human Disease

To assess whether MYC-driven tumorigenesis was associated with metastases, we collected liver and lymph nodes from tumor-bearing RPM mice at 8 weeks and RPP mice at 24 weeks to control for the amount of primary tumor burden in each genotype. Mediastinal spread via lymphatics and blood-borne metastases in the liver were prominent in RPM mice (Figures 4A and 4B). Out of 16 livers from RPM mice, 14 (~88%) exhibited liver metastases, often presenting with multiple micro-metastases (Figures 4A and 4C). Remarkably, clusters of tumor cells were identified in the blood vessels of the liver, and were proliferating as demonstrated by multiple mitotic cells (Figure 4A). Despite the much longer time frame for tumor development, significantly fewer RPP animals demonstrated liver metastases (36%) (Figure 4C). Fifteen out of 21 RPM mice (~71%) also exhibited metastases to mediastinal and distant lymph nodes (Figure 4B and data not shown). Metastases were highly proliferative based on Ki67 staining and stained strongly for NKX2-1 and UCHL1 (Figure 4D), consistent with a lung neuroendocrine origin. RPM tumors also exhibited high levels of the metastatic driver NFIB in both primary tumors and metastases (Figures 4D and 4E), but did not exhibit *Nfib* amplifications that are commonly found in MYCL-driven SCLC (Figure S2A) (Denny et al., 2016; Dooley et al., 2011; Semenova et al., 2016). However, consistent with high homogeneous NFIB expression in primary tumors (Figure 4E), *Nfib* was identified as an MYC target gene by ChIP-seq in RPM cell lines (Figure 4F). This suggests that MYC directly regulates *Nfib*, which may contribute to rapid metastases. Thus, the metastatic pattern of MYC-driven mouse SCLC resembles human SCLC and occurs much more rapidly than in other classic GEMMs (McFadden et al., 2014; Meuwissen et al., 2003; Schaffer et al., 2010).

MYC-Driven SCLC Is Responsive to Chemotherapy but Rapidly Relapses

The influence of MYC on chemotherapy response in SCLC is controversial and has not been explored in vivo to our knowledge (Hodgkinson et al., 2014; Johnson et al., 1987). To address this, we treated RPM and RPP mice with or without a single dose of 7 mg/kg cisplatin (day 1) and 10 mg/kg etoposide (day 2) followed by a single 24 hr pulse of bromodeoxyuridine, and collected lung tissue for IHC analyses. Untreated tumors of both genotypes exhibited detectable DNA damage measured by levels of phospho-histone H2A.X (pH2AX) (Figure 5A). In response to chemotherapy, RPM and RPP tumors exhibited a significant increase in pH2AX as expected (Figures 5A and 5B). In contrast to adenocarcinomas that exhibit a strong cell-cycle arrest following chemotherapy (Oliver et al., 2010), neither RPM nor RPP tumors exhibited reduced proliferation (Figures 5A and 5C). Instead, chemotherapy-treated RPM tumors had significantly increased levels of CC3 compared with untreated controls, which was not observed in RPP tumors (Figures 5A and 5D). Together, this suggests that high levels of DNA damage coupled with a failure to arrest the cell cycle leads to apoptotic cell death in RPM tumors.

Because of the dramatic response to a single dose of chemotherapy, we sought to determine whether chemotherapy could reduce tumor burden in RPM animals. We treated a cohort of RPM mice with two doses of combination chemotherapy (5 mg/kg cisplatin and 10 mg/kg etoposide) or vehicle control and harvested lung tissue 72 hr after the second dose. RPM tumors treated with chemotherapy exhibited dramatically reduced tumor burden (3.8% ± 1.6%) compared with control animals (19.5% ± 3.1% tumor burden) (Figures 5E and S4), indicating that MYC-driven tumors are indeed chemo-sensitive. MicroCT imaging provides a more comprehensive assessment of tumor burden, so we also quantified tumor burden before treatment at day 0 and again on day 12 following two doses of chemotherapy. PBS-treated tumors grew significantly from 12% to 35% tumor burden in only 12 days, whereas chemotherapy-treated tumors had minor increases from 12% to 17% tumor burden that were not statistically significant (Figure 5F). We observed heterogeneity in the response of individual tumors including progression, stasis, and regression (data not shown). In another cohort of RPM mice, combination chemotherapy significantly prolonged survival, but the overall added survival benefit was only 10.5 days (Figure 5G). The majority of lungs from RPM mice receiving repeated chemotherapy still harbored tumors (Figure S4), suggesting that they had possibly acquired resistance to chemotherapy. These data suggest that RPM tumors accurately reflect the clinical response of human SCLC. While MYC alone does not confer chemo-resistance per se, MYC-driven tumors rapidly relapse following treatment. This prompted us to search for targeted therapies that could improve chemotherapy response.

MYC-Driven SCLC Is Vulnerable to Aurora Kinase Inhibition

Despite numerous efforts, MYC remains difficult to target with small molecules. However, a number of synthetic lethal targets have been identified in MYC-driven tumors that may provide therapeutically exploitable vulnerabilities (Brockmann et al., 2013; Bunn et al., 2016; Sos et al., 2012; Toyoshima et al., 2012; Yang et al., 2010). To assess the efficacy of drugs that inhibit such candidate synthetic lethal targets, we profiled the activity of etoposide, cisplatin, PF-670462 (CKIε inhibitor),

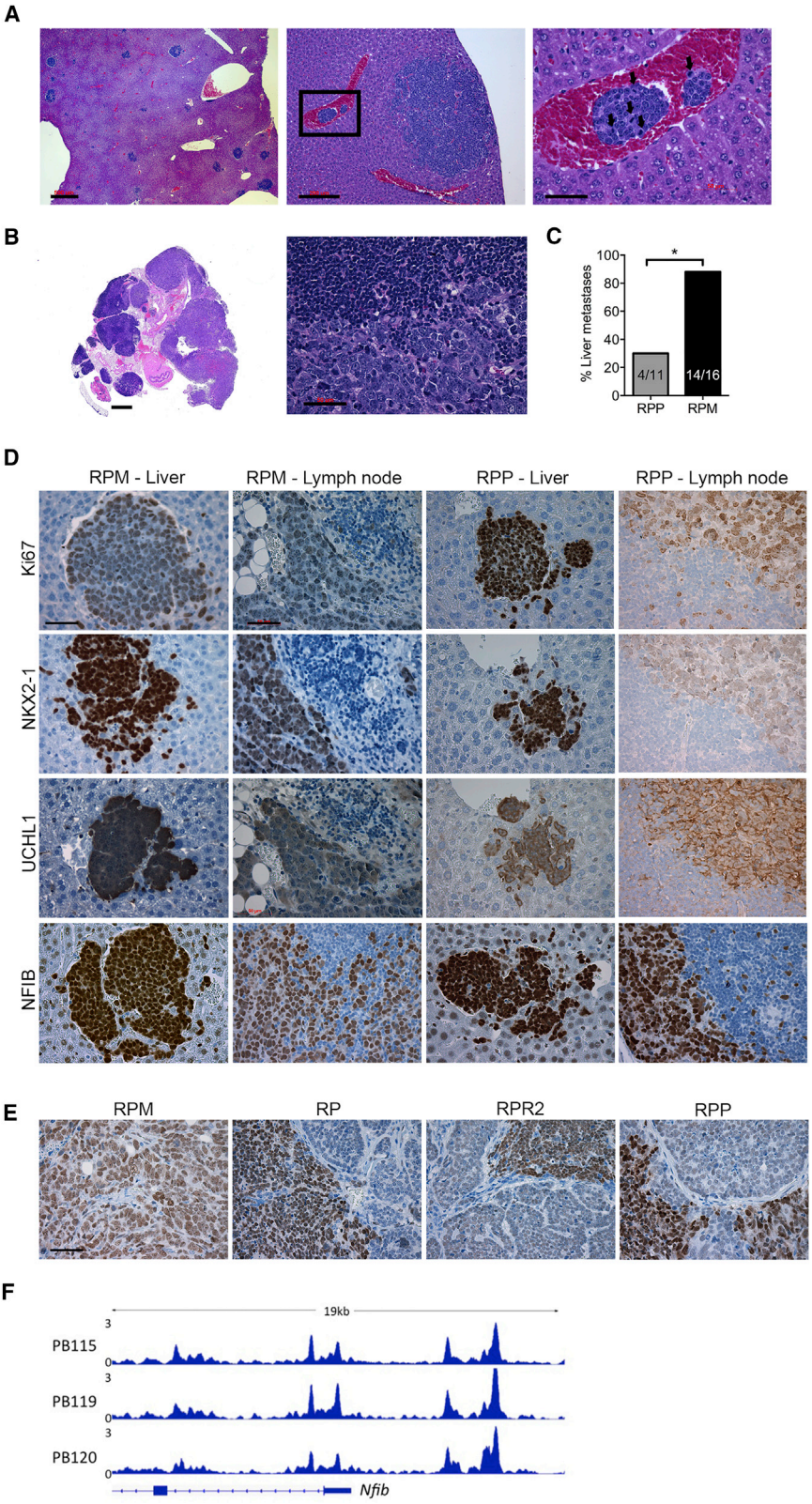

Figure 4. MYC-Driven Tumors Are Highly Metastatic Similar to the Human Disease

(A) Representative H&E stains of metastatic liver lesions from RPM mice. The area in the black box of the middle panel is magnified in the right panel. Black arrows indicate mitotic figures in the blood vessel. Scale bars, 500, 200, and 50 μm.

(B) H&E image of mediastinal lymph node metastases from RPM mice. Scale bars, 1 mm and 50 μm.

(C) Percentage of mice with liver metastases analyzed by a contingency table with Fisher's exact test, two-tailed, *p = 0.0115. The number of mice with liver metastases out of the total number of mice is indicated within bars.

(D) Representative IHC for indicated antibodies in metastatic tissues from RPM or RPP mice. Scale bar, 50 μm.

(E) Representative IHC for NFIB in primary lung tissue from indicated mice. Scale bar, 50 μm.

(F) ChIP-seq analysis of MYC targets in three independent RPM cell lines with exons of *Nfib* gene indicated by rectangles at the bottom.

MS436 (BRD4 inhibitor), Alisertib (Aurora A inhibitor), Barasertib (Aurora B inhibitor), and Milciclib (CDK2 inhibitor) across 17 human SCLC cell lines (Figure 6A). *MYC*-amplified SCLCs were significantly more responsive to etoposide (adjusted p = 0.038), Alisertib (p = 0.001), and Barasertib (p = 0.022) compared with those with *MYCL* or *MYCN* amplifications (Figure 6B). We also analyzed a recently published drug screen including 68 human SCLC cell lines by binning cells based on high or low *MYC* expression (Polley et al., 2016). Again, Alisertib, Barasertib, and multiple other Aurora kinase inhibitors exhibited increased efficacy in *MYC*-high cell lines (Figure S5A). Next, we generated mouse cell lines from RPM tumors including five from RPM mice and two from $RPM^{LSL/+}$ mice. Cells grew largely in suspension, often in loose aggregates or clusters similar to human variant SCLC cell lines (Figure S5B). RPM cell lines expressed high levels of MYC and did not express RB1 or TRP53 (Figure S5C). Next, we treated RPM, $RPM^{LSL/+}$, RPP, RP, and KP cell lines with cisplatin, etoposide, Alisertib, or Barasertib. RPM cells exhibited high micromolar GI50 (50% growth inhibition) in response to cisplatin, but were highly sensitive to etoposide at nanomolar concentrations (Figures 6C and 6D). RPM cells were particularly sensitive to Alisertib and Barasertib when compared with adenocarcinoma cell lines and non-MYC-driven cells (Figures 6E–6G). RPM cells tended to have a shorter doubling time, but there was not a significant correlation between doubling time and Alisertib sensitivity (Figure S5D). Alisertib treatment resulted in

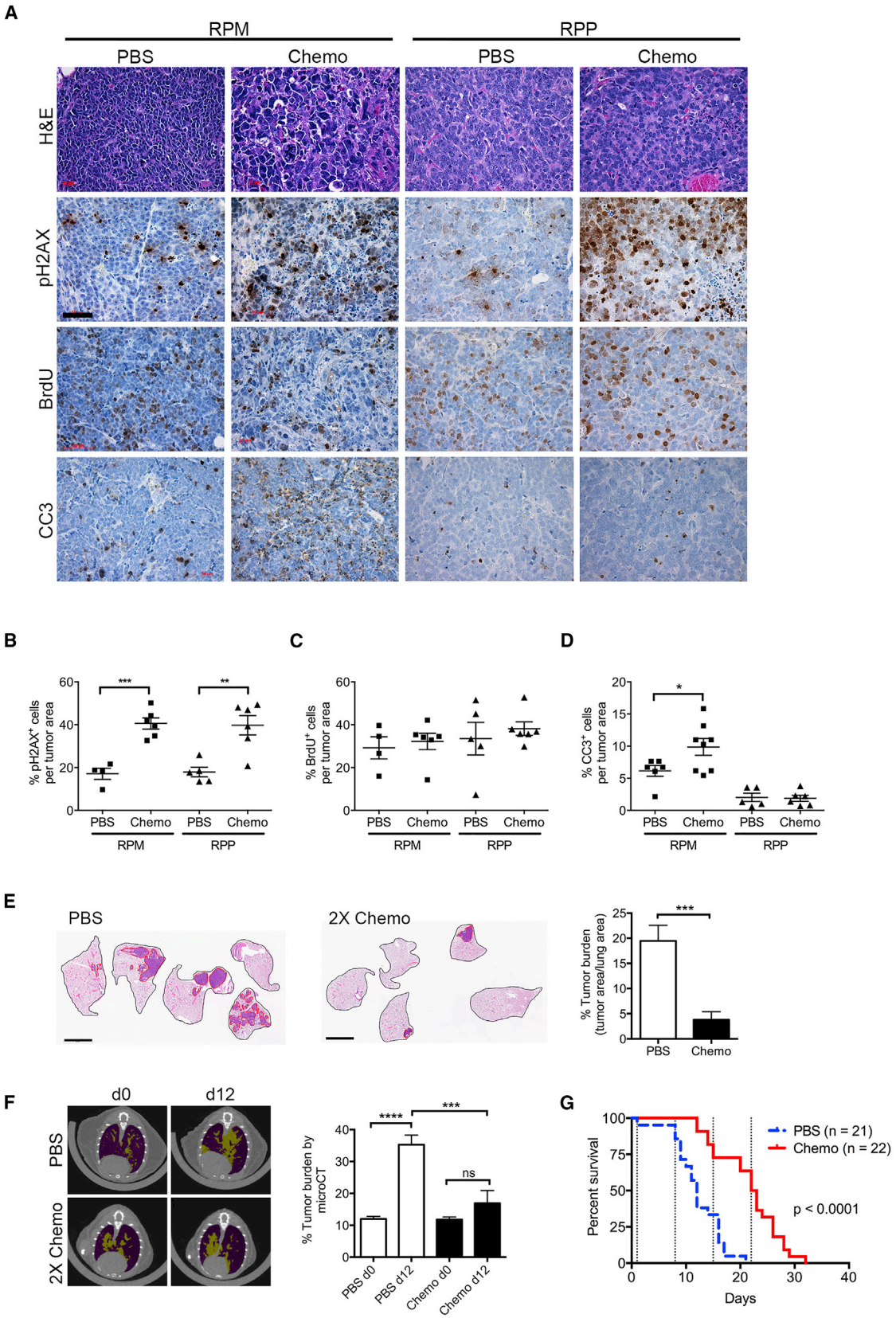

(legend on next page)

dose-dependent inhibition of AURKA and AURKB at concentrations in the range of the determined GI_{50} value in mouse and human cells, while Barasertib was highly specific for AURKB (Figures 6H, S5E, and S5F). In *MYC*-amplified GLC2 cells we observed a reduction in viability after knock down of AURKA and of AURKB, implying that inhibition of AURKB could also play a role in the reduced viability of Alisertib-treated cells (Figure S5G). In RPM cells, Alisertib caused a dose-dependent increase in G2/M phase cells followed by an increase in subG1 cells, suggesting that cells fail to properly exit mitosis and die thereafter (Figure 6I). Compared with KP, RPP, and RP cells, RPM cells exhibited a greater increase in subG1 cells following Alisertib treatment (Figure 6I). In contrast to described mechanisms of Aurora kinase inhibition in other malignancies (Brockmann et al., 2013; Otto et al., 2009), Alisertib treatment did not primarily lead to reduced MYC protein in mouse or human cells (Figures 6H, S5E, and S5F), even after cycloheximide-induced block of protein synthesis (Figure S5H). As expected, MYC was more stable in mouse cells expressing MYC^{T58A} (PB115), when compared with MYC^{WT} cells (GLC1) (Figure S5H). However, in both cell lines, we did not observe a robust decrease of MYC after Alisertib treatment compared with control cells, suggesting that MYC^{T58A} likely does not alter the mechanistic basis of Alisertib sensitivity (Figure S5H). While the effect of Alisertib treatment was pronounced in vitro, the combination of Alisertib with etoposide, but not cisplatin, further decreased cell viability in *MYC*-amplified cells (Figure S5I). This suggests that MYC-driven SCLC is highly sensitive to Aurora kinase inhibition in mouse and human cells independent of proliferation rate and its impact on MYC levels.

Aurora Kinase Inhibition Significantly Improves the Chemotherapy Response of MYC-Driven SCLC

To determine the efficacy of Alisertib in vivo, RPM mice were imaged by microCT and, upon detection of tumors, randomly assigned to receive either vehicle control (PBS), chemotherapy (cisplatin and etoposide), Alisertib, or chemotherapy plus Alisertib (Figure 7A). Mice were imaged immediately before treatment and 4 days after each cisplatin treatment for up to 20 days. Weight loss upon Alisertib treatment did not differ from PBS-treated animals, but regimens with chemotherapy caused ~15%–20% weight loss such that one animal in each treatment group had to be killed due to toxicity (Figure S6A). We quantified total tumor volume relative to total air volume as a comprehensive measurement of treatment impact. PBS-treated animals exhibited rapid tumor growth within 12 days following tumor detection (Figures 7B, 7C, and S6B). Alisertib-treated animals exhibited a modest delay in tumor growth, which was largely attributable to its impact at early time points. The majority of chemotherapy-treated animals completed three cycles of therapy with significantly delayed tumor growth (Figures 7B, 7C, and S6B). Strikingly, the majority of animals treated with a combination of Alisertib and chemotherapy exhibited complete tumor stasis over three cycles of treatment (Figures 7B, 7C, and S6B). We analyzed the percent change in total tumor volume at day 19 (or at the time of death if sooner) compared with day 0 in each treatment group by waterfall plot. Despite the initial delay in tumor growth, Alisertib alone did not impact overall response compared with untreated animals in this time frame (Figure 7D). Of chemotherapy-treated animals, 5 of 14 experienced stable disease, while the majority of animals (n = 9 of 14) progressed during treatment. Remarkably, the majority of animals treated with chemotherapy and Alisertib (n = 10 of 16) exhibited stable disease including three animals with >30% reduction in tumor volume (Figure 7D).

Given the heterogeneity in classic and variant cells in the RPM model, we sought to determine whether these treatments impact ASCL1, NEUROD1, or MYC levels. Interestingly, chemotherapy led to a reduction in ASCL1 levels, suggesting that the classic or early-stage lesions may be more chemo-sensitive in this model (Figures 7E and 7F). Most strikingly, Alisertib treatment led to a dramatic enrichment of cells with polyploidy and aberrant mitoses (Figure S6C) consistent with its mechanism of action (Wilkinson et al., 2007). These abnormal cells were $NEUROD1^{+}$ and significantly enriched in Alisertib-treated animals compared with other treatment groups (Figures 7E, 7F, and S6C). The combination of Alisertib with chemotherapy, however, did not lead to enrichment of $NEUROD1^{+}$ cells, suggesting that chemotherapy may have contributed to the depletion of these large aberrant cells. MYC levels were not significantly altered in any treatment group compared with untreated tumors (Figure 7F).

Despite the modest delay in tumor growth, Alisertib treatment increased median survival by 10 days compared with untreated animals, comparable with chemotherapy, which increased survival by 11 days (Figure 7G). The combination of chemotherapy with Alisertib increased median survival by 14 days compared with untreated mice and was significantly more efficacious than either Alisertib or chemotherapy alone. Importantly, 47% of combination-treated mice survived 30 days compared with 0%, 5%, and 8% of the PBS, chemo-, or Alisertib-treated animals (Fisher's exact test p = 0.0008, 0.0032, and 0.0433, respectively). These results suggest that Alisertib with chemotherapy in first-line treatment of MYC-driven SCLC halts tumor growth and significantly extends survival compared with the standard-of-care chemotherapy.

Figure 5. MYC-Driven SCLC Is Highly Responsive to Chemotherapy but Rapidly Relapses

(A) H&E-stained lung tumor tissue from RPM or RPP mice in the absence (PBS) or presence of a single dose of chemotherapy (Chemo) and representative IHC for indicated antibodies. Scale bar, 50 μm.

(B–D) Automated quantification of IHC for pH2AX (B), bromodeoxyuridine (BrdU) (C), or CC3 (D) from mice as in (A). Dots are average per animal. ***p < 0.0003, **p < 0.003, *p < 0.05.

(E) H&E of whole lung sections from RPM mice treated with PBS or two doses of chemotherapy (2× Chemo). Lung outlined in black, tumor outlined in red. Scale bar, 4 mm. Automated quantification of percent tumor burden; n = 7 mice per treatment group. ***p < 0.0007.

(F) Representative microCT images and quantification of total tumor burden from animals in (E) at day 0 (d0) or day 12 (d12). Tumors are pseudo-colored yellow; air space is purple. ***p < 0.0008, ****p < 0.0001. For (B), (C), (D), (E), and (F), error bars indicate mean ± SEM with two-tailed unpaired t tests.

(G) Kaplan-Meier survival analysis of RPM mice treated with 5 mg/kg cisplatin and 10 mg/kg etoposide indicated by dashed vertical lines. Log rank (Mantel-Cox) test indicated. See also Figure S4.

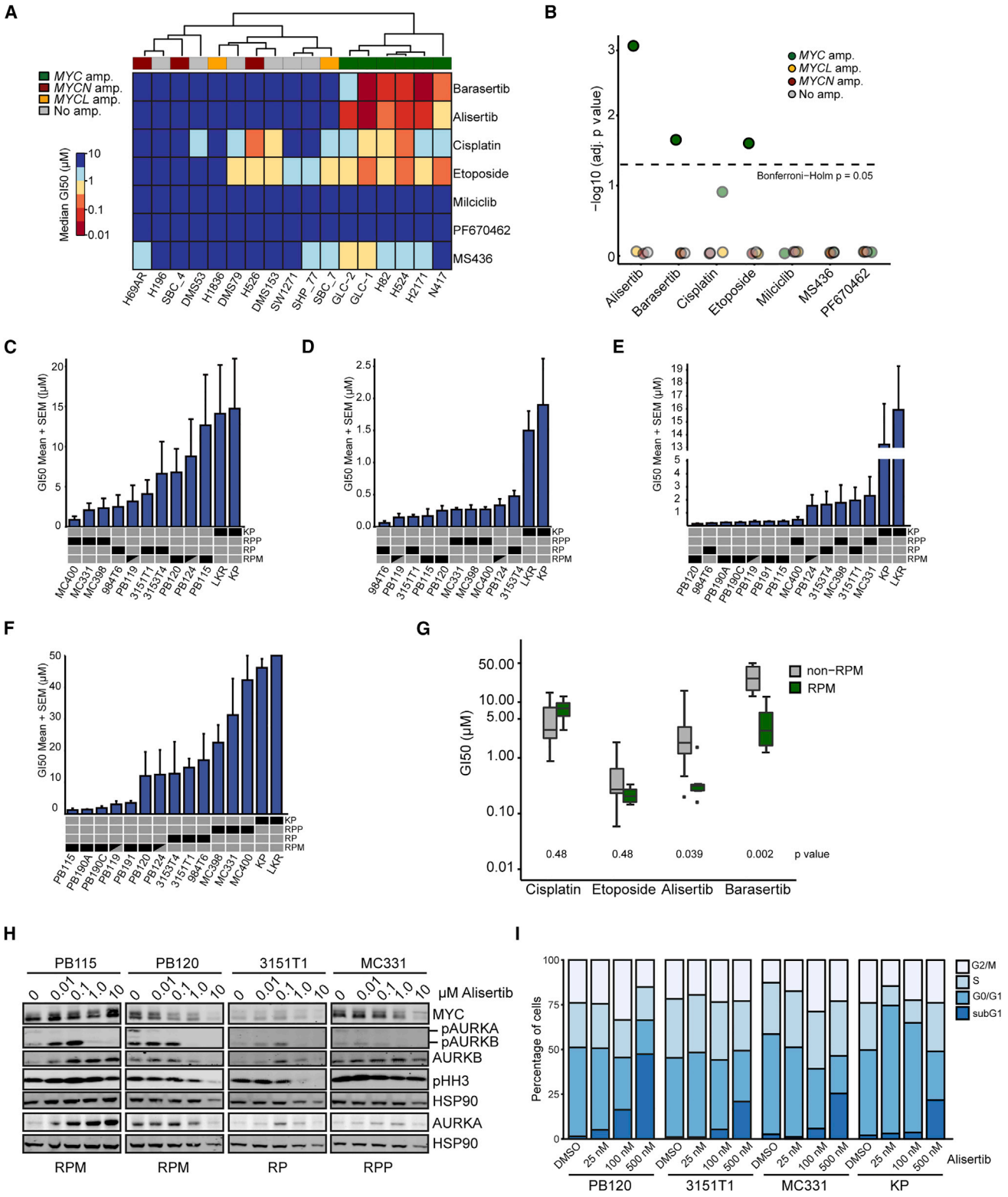

Figure 6. MYC-Driven SCLC Is Vulnerable to Aurora Kinase Inhibition

(A) Heatmap of median GI_{50} values for indicated human SCLC cell lines treated with indicated drugs for 72–96 hr.

(B) Statistical significance of increased drug responses in (A) tested for each compound (one-sided t tests, p values adjusted according to Bonferroni-Holm).

(C–F) GI_{50} values of cells treated with cisplatin (C), etoposide (D), Alisertib (E), or Barasertib (F) in triplicate for 96 hr. Mean ± SEM of n = 4–7 experiments. Black boxes indicate genotype; half black boxes indicate $RPM^{LSL/+}$.

(legend continued on next page)

DISCUSSION

Over 30 years ago, human SCLC cell lines with variant morphology were found to exhibit frequent *MYC* amplifications (Carney et al., 1985; Gazdar et al., 1985). Here we show that MYC drives the variant histopathology in vivo, a subset of tumors that has not been previously observed in GEMMs (Gazdar et al., 2015). Our data suggest this is likely because *Mycl* is the oncogenic driver in other GEMMs (Calbo et al., 2011; Dooley et al., 2011), whereas *Myc* serves this function in our model. Importantly, we find that MYC promotes a neuroendocrine-low phenotype associated with high expression of NEUROD1. *NEUROD1* expression was initially found to correlate with the variant subtype of cell lines (Poirier et al., 2013) and was subsequently found to stratify a subset of *ASCL1*^{low} primary human SCLCs in multiple studies (Borromeo et al., 2016; Poirier et al., 2015). NEUROD1 is present along with MYC at super-enhancers in *MYC*-high cell lines (Borromeo et al., 2016; Christensen et al., 2014). Thus far, it appears that normal mouse neuroendocrine cells do not express *Neurod1*, so it has been questioned whether *NEUROD1*-expressing human tumors arise in the lung or metastasize from elsewhere in the body (Borromeo et al., 2016; Bunn et al., 2016). We show that murine MYC-driven SCLCs express NEUROD1 and have a significantly higher *NEUROD1* signature than other GEMMs, suggesting that their human counterparts arise in the lung. Based on in situ immunostaining patterns for ASCL1 and NEUROD1, we postulate that MYC-driven tumor cells arise in ASCL1^{+} precursors, and these early tumor cells initially exhibit classic morphology. With time, it appears that tumors switch to an ASCL1^{low}/NEUROD1^{high} state coincident with the appearance of variant morphology and neuroendocrine-low phenotype. Since overexpression of NEUROD1 has been linked to the development of metastases and aggressive SCLC (Osborne et al., 2013), our data suggest that MYC activation could fuel this phenotype via NEUROD1 signaling. Our data suggest MYC's role in NEUROD1 regulation may be indirect given the absence of NEUROD1 expression in in situ lesions that are MYC^{+}. Given the essential role of ASCL1 in MYCL-driven tumors (Borromeo et al., 2016), further studies are warranted to address the role of ASCL1 and NEUROD1 in MYC-driven tumors. These data have important clinical implications given the recent development of neuroendocrine gene-targeted therapies, such as the DLL3-antibody drug conjugate (Saunders et al., 2015). Our data predict that MYC-driven SCLCs with low neuroendocrine gene expression may be relatively less responsive to some neuroendocrine-targeted therapies.

There is an urgent need for SCLC models that recapitulate the key clinical aspects of the human disease. The short latency of SCLC development in RPM mice will greatly facilitate preclinical therapeutic studies in SCLC. MYC-driven SCLCs also rapidly develop metastases to the lymph nodes and liver with frequencies similar to the human disease, and in manageable time frames for studying mechanisms of metastasis including the role of NFIB. Because the RPM mice are immunocompetent, they will complement other immunodeficient SCLC models such as PDXs derived from tissue or circulating tumor cells (Hodgkinson et al., 2014).

One of the major clinical barriers to SCLC treatment is the development of chemotherapy resistance. Like human SCLC, RPM tumors demonstrate acute sensitivity to chemotherapy, suggesting that MYC alone is not sufficient to promote chemoresistance. However, it is not yet clear whether ASCL1^{+} or NEUROD1^{+} components have differential sensitivities to chemotherapy, so further studies to address the heterogeneity in treatment response of MYC-driven tumors is warranted. Our findings suggest that MYC's role in tumor progression is to promote aggressive proliferation and metastases, but its role in chemoresistance requires further investigation. The RPM GEMM will serve as a useful tool for uncovering mechanisms of chemoresistance and for testing therapeutic strategies to combat chemo-resistant disease.

MYC-driven tumors, including SCLCs, exhibit synthetic lethality with Aurora kinase inhibition, but this had not been explored in SCLC GEMMs in vivo (Brockmann et al., 2013; Gustafson et al., 2014; Hook et al., 2012; Otto et al., 2009; Sos et al., 2012; Yang et al., 2010). Our data suggest that MYC sensitizes SCLC to Aurora kinase inhibition particularly in combination with chemotherapy, which significantly improved tumor control and prolonged survival compared with chemotherapy alone. Alisertib monotherapy had only modest impact in vivo, but it remains possible that an optimized dosing regimen could improve this response. Recent clinical trials in relapsed SCLC tested Alisertib monotherapy, with ~20% of patients exhibiting partial responses (Melichar et al., 2015), while a pan-Aurora kinase inhibitor had no responses in a small number of relapsed patients (Schoffski et al., 2015). Current clinical trials are assessing Alisertib in combination with chemotherapy as a second-line therapy (NCT02038647). Our data predict that MYC levels, a neuroendocrine-low expression profile, or variant histopathology may serve as biomarkers for sensitivity to Aurora kinase inhibition in patients. Finally, our data suggest that Aurora kinase inhibition can improve chemotherapy response in vivo, suggesting that patients with *MYC*-amplified SCLCs may benefit from first-line Aurora kinase inhibitors in combination with standard chemotherapy. Together these findings challenge the current classification of SCLC as a homogeneous disease and suggest that distinct subtypes of SCLC exist with specific vulnerabilities to targeted therapies that are poised to improve patient outcomes.

EXPERIMENTAL PROCEDURES

Mice

Mice were housed in an environmentally controlled room and all experiments were performed in accordance with University of Utah's Institutional Animal Care and Use Committee. *p53*$^{fl/fl}$ mice were generated by A. Berns (Meuwissen et al., 2003) and RP mice were provided by T. Jacks (Sage et al., 2003). RPP mice were provided by D. MacPherson (Cui et al., 2014). RPM mice will

(G) GI_{50} drug responses of SCLC cell lines grouped according to *MYC* status. p values were calculated by two-sided t tests with Bonferroni-Holm correction for multiple testing.

(H) Immunoblot of whole-cell lysates from cell lines treated for 48 hr with indicated concentrations of Alisertib. HSP90 serves as loading control.

(I) DNA content of PB120 (RPM), 3151T1 (RP), MC331 (RPP), and KP mouse cell lines treated with Alisertib (48 hr) measured by flow cytometry, representative of n = 2 experiments.

See also Figure S5.

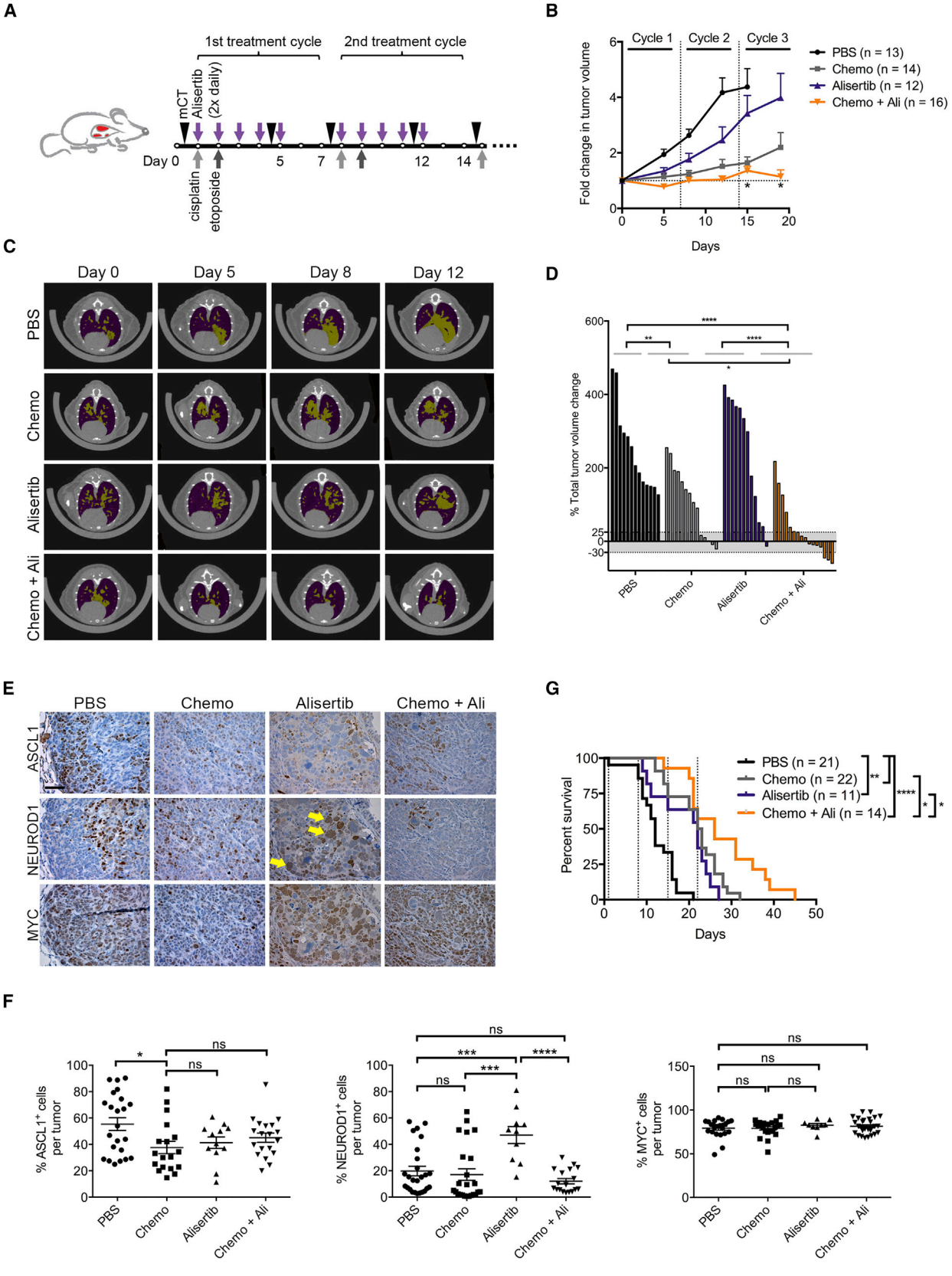

(legend on next page)

be available at The Jackson Laboratory as stock no. 029971. At 6–8 weeks of age, anesthetized mice were infected with 10^6–10^8 plaque-forming units of Ad5-Cgrp-Cre viruses (University of Iowa) by intratracheal instillation as described elsewhere (Jackson et al., 2001). Viruses were administered in a Biosafety Level 2+ room according to Institutional Biosafety Committee guidelines. Both male and female mice were equally divided between treatment groups for all experiments.

MicroCT and Bioluminescent Imaging

Mice were scanned for 34 s under isoflurane anesthesia using a small animal Quantum FX microCT (PerkinElmer) at 45 μm resolution, 90 kV, with 160 μA current. Images were acquired using PerkinElmer Quantum FX software and processed with Analyze 11.0 (AnalyzeDirect). For bioluminescent imaging, mice were shaved and given 150 mg/kg D-luciferin potassium salt (Regis Technologies) intraperitoneally and imaged on a Xenogen IVIS Spectrum instrument (PerkinElmer).

IHC

Lungs were inflated with PBS or formalin, fixed overnight in neutral buffered formalin, and transferred to 70% ethanol. Paraffin-embedded lung lobes were sectioned at 4 μm and stained with H&E for tumor pathology or with antibodies as described previously (Mukhopadhyay et al., 2014).

Human Genomics

RNA-seq data for human patient samples and cell lines were obtained from published literature (George et al., 2015; Peifer et al., 2012; Rudin et al., 2012) and newly generated datasets with gene expression quantified as fragments per kilobase per million reads (FPKM) and analyses performed on $\log_2$(FPKM + 1).

Statistics

Boxplots represent 25th and 75th percentiles with midline indicating the median; whiskers extend to the lowest/highest value within 1.5 times the interquartile range. Outliers are shown as dots.

ACCESSION NUMBERS

Mouse lung tumor RNA-seq data (GEO: GSE89660) and mouse ChIP-seq cell line data (GEO: GSE87034) in this study are deposited in the NCBI GEO. Human SCLC cell line RNA-seq data generated in this study are deposited at www.ebi.ac.uk/ega (EGAS00001002115).

SUPPLEMENTAL INFORMATION

Supplemental Information includes Supplemental Experimental Procedures, six figures, and one table and can be found with this article online at http://dx.doi.org/10.1016/j.ccell.2016.12.005.

AUTHOR CONTRIBUTIONS

Conceptualization, T.G.O., M.L.S., R.J.W.-R., A.F.G., and J.E.J.; Methodology, M.E.S.; Formal Analysis, T.L.M., S.B., J.B., A.M., J.G., C.H., J.L.K., J.M.V., J.G., M.E.S., B.L.W., A.F.G., and T.G.O.; Investigation, G.M., M.R.G., S.B., J.B., A.M., P.M.B., I.C., H.C., M.D.C., A.S.I., J.G., C.H., K.E.D., T.L.M., J.W., A.M., K.C.B., J.M.V., M.P., R.K.T., J.E.J., A.F.G., M.L.S., and T.G.O.; Pathology, A.F.G., B.L.W., and M.E.S.; Resources, R.J.W.-R.; Data Curation, J.B. and T.L.M.; Writing – Original Draft, T.G.O.; Writing – Review & Editing, G.M., M.R.G., S.B., J.B., T.L.M., J.E.J, A.F.G., R.J.W.-R., R.K.T., M.L.S., and T.G.O.; Supervision, T.G.O., M.L.S., R.K.T., R.J.W.-R., J.E.J., and A.F.G.; Project Administration, T.G.O. and R.J.W.-R.; Funding Acquisition, T.G.O., M.L.S., R.K.T., M.P., J.E.J., A.F.G., and R.J.W.-R.

ACKNOWLEDGMENTS

Thanks to K. Sutherland and A. Berns for permission to use Cgrp-Cre viruses; for RP mice provided by T. Jacks and A. Berns, RPP mice and RP tissues from D. MacPherson, and RPR2 tissues from J. Sage. We appreciate technical assistance from members of the Oliver Lab including M. Baladi, B. Anderson, and K. Gligorich for histological services, and B. Dalley for bioinformatics support. Thanks to E. Snyder for critical reading of the manuscript. T.G.O. was supported in part by a V Scholar award from The V Foundation for Cancer Research, the American Cancer Society (Research Scholar Award no. RSG-13-300-01-TBG), and the NIH (no. R01CA187457-01). T.G.O. is a Damon Runyon-Rachleff Innovation Awardee and this work is supported by the Damon Runyon Cancer Research Foundation (no. DRR-26-13). A.M. is supported by the Köln Fortune Research Scholar Award and J.E.J. by CPRIT RP140143. M.L.S. was supported by the EFRE initiative (no. LS-1-1-030a to R.K.T. and M.L.S), German Ministry of Science and Education (BMBF) as part of the e:Med program (no. 01ZX1303 to R.K.T., M.P. and no. 01ZX1406 to M.L.S, M.P.), Deutsche Forschungsgemeinschaft (no. TH1386/3-1 to R.K.T and M.L.S.), and received a commercial research grant from Novartis. Funding to R.K.T. was also provided by the German Cancer Aid (Deutsche Krebshilfe, no. 109679), SFB832 (TP6), Deutsche Krebshilfe as part of Oncology Centers of Excellence, EU-Framework program CURELUNG (HEALTH-F2-2010-258677), PerMed.NRW initiative (no. 005-1111-0025), Stand Up To Cancer—American Association of Cancer Research Innovative Research Grant (SU2C-AACR-IR60109), and German Consortium for Translational Cancer Research Joint Funding program. R.K.T. received commercial research grants (AstraZeneca, EOS, Merck KgaA) and honoraria (AstraZeneca, Bayer, NEO New Oncology AG, Boehringer Ingelheim, Clovis Oncology, Daiichi-Sankyo, Eli Lilly, Johnson & Johnson, Merck KgaA, MSD, Puma, Roche, Sanofi). M.P. is a scientific consultant of NEO New Oncology AG.

Received: May 31, 2016
Revised: September 15, 2016
Accepted: December 13, 2016
Published: January 12, 2017

REFERENCES

Borromeo, M.D., Savage, T.K., Kollipara, R.K., He, M., Augustyn, A., Osborne, J.K., Girard, L., Minna, J.D., Gazdar, A.F., Cobb, M.H., and Johnson, J.E. (2016). ASCL1 and NEUROD1 reveal heterogeneity in pulmonary neuroendocrine tumors and regulate distinct genetic programs. Cell Rep. *16*, 1259–1272.

Brennan, J., O'Connor, T., Makuch, R.W., Simmons, A.M., Russell, E., Linnoila, R.I., Phelps, R.M., Gazdar, A.F., Ihde, D.C., and Johnson, B.E. (1991). myc

Figure 7. Aurora Kinase Inhibition Combined with Chemotherapy Significantly Prolongs Survival of Mice with MYC-Driven SCLC

(A) Schematic for in vivo drug studies in RPM mice. Black arrowheads indicate microCT imaging (mCT). Purple arrows indicate Alisertib (Ali) treatment (20 mg/kg, twice daily, 5 days on, 2 days off); gray arrows indicate cisplatin (5 mg/kg) or etoposide (10 mg/kg) (Chemo, weekly). Days indicated as white dots on the x axis.

(B) Fold change in tumor burden in indicated cohorts of RPM mice. Error bars represent mean ± SEM. For Chemo versus Chemo + Ali, *p < 0.05 at indicated time points.

(C) Representative microCT images from RPM mice pseudo-colored with tumors (yellow) and normal tissue/airway (purple).

(D) Total tumor volume change from days 0 to 19 (or last scan before death) of individual RPM mice treated as in (A) for three cycles. Partial response and stable disease indicated with gray shading. Two-tailed unpaired t tests, *p < 0.023, **p < 0.002, ****p < 0.0001.

(E and F) IHC for indicated antibodies in each treatment group (E) and automated quantification of IHC (F). Scale bar, 50 μm. Abnormal NEUROD1$^+$ cells are indicated by yellow arrows. Error bars represent mean ± SEM, two-tailed unpaired t tests, *p < 0.02, ***p < 0.0008, ****p < 0.0001. ns, not significant.

(G) Kaplan-Meier survival analysis of RPM mice treated as in (A) with day 0 as start of treatment and cisplatin treatment indicated by dashed lines. Log rank (Mantel-Cox) test, *p < 0.02, **p < 0.009, ****p < 0.0001. ns, not significant.

See also Figure S6.

family DNA amplification in 107 tumors and tumor cell lines from patients with small cell lung cancer treated with different combination chemotherapy regimens. Cancer Res. *51*, 1708–1712.

Brockmann, M., Poon, E., Berry, T., Carstensen, A., Deubzer, H.E., Rycak, L., Jamin, Y., Thway, K., Robinson, S.P., Roels, F., et al. (2013). Small molecule inhibitors of Aurora-a induce proteasomal degradation of N-myc in childhood neuroblastoma. Cancer Cell *24*, 75–89.

Bunn, P.A., Jr., Minna, J., Augustyn, A., Gazdar, A., Ouadah, Y., Krasnow, M.A., Berns, A., Brambilla, E., Rekhtman, N., Massion, P.P., et al. (2016). Small cell lung cancer: can recent advances in biology and molecular biology be translated into improved outcomes? J. Thorac. Oncol. *11*, 453–474.

Calbo, J., van Montfort, E., Proost, N., van Drunen, E., Beverloo, H.B., Meuwissen, R., and Berns, A. (2011). A functional role for tumor cell heterogeneity in a mouse model of small cell lung cancer. Cancer Cell *19*, 244–256.

Carney, D.N., Gazdar, A.F., Bepler, G., Guccion, J.G., Marangos, P.J., Moody, T.W., Zweig, M.H., and Minna, J.D. (1985). Establishment and identification of small cell lung cancer cell lines having classic and variant features. Cancer Res. *45*, 2913–2923.

Christensen, C.L., Kwiatkowski, N., Abraham, B.J., Carretero, J., Al-Shahrour, F., Zhang, T., Chipumuro, E., Herter-Sprie, G.S., Akbay, E.A., Altabef, A., et al. (2014). Targeting transcriptional addictions in small cell lung cancer with a covalent CDK7 inhibitor. Cancer Cell *26*, 909–922.

Cui, M., Augert, A., Rongione, M., Conkrite, K., Parazzoli, S., Nikitin, A.Y., Ingolia, N., and MacPherson, D. (2014). PTEN is a potent suppressor of small cell lung cancer. Mol. Cancer Res. *12*, 654–659.

Denny, S.K., Yang, D., Chuang, C.H., Brady, J.J., Lim, J.S., Gruner, B.M., Chiou, S.H., Schep, A.N., Baral, J., Hamard, C., et al. (2016). Nfib promotes metastasis through a widespread increase in chromatin accessibility. Cell *166*, 328–342.

Dooley, A.L., Winslow, M.M., Chiang, D.Y., Banerji, S., Stransky, N., Dayton, T.L., Snyder, E.L., Senna, S., Whittaker, C.A., Bronson, R.T., et al. (2011). Nuclear factor I/B is an oncogene in small cell lung cancer. Genes Dev. *25*, 1470–1475.

Elliott, J.A., Osterlind, K., Hirsch, F.R., and Hansen, H.H. (1987). Metastatic patterns in small-cell lung cancer: correlation of autopsy findings with clinical parameters in 537 patients. J. Clin. Oncol. *5*, 246–254.

Gazdar, A.F., Carney, D.N., Nau, M.M., and Minna, J.D. (1985). Characterization of variant subclasses of cell lines derived from small cell lung cancer having distinctive biochemical, morphological, and growth properties. Cancer Res. *45*, 2924–2930.

Gazdar, A.F., Savage, T.K., Johnson, J.E., Berns, A., Sage, J., Linnoila, R.I., MacPherson, D., McFadden, D.G., Farago, A., Jacks, T., et al. (2015). The comparative pathology of genetically engineered mouse models for neuroendocrine carcinomas of the lung. J. Thorac. Oncol. *10*, 553–564.

Gazzeri, S., Brambilla, E., Jacrot, M., Chauvin, C., Benabid, A.L., and Brambilla, C. (1991). Activation of myc gene family in human lung carcinomas and during heterotransplantation into nude mice. Cancer Res. *51*, 2566–2571.

George, J., Lim, J.S., Jang, S.J., Cun, Y., Ozretic, L., Kong, G., Leenders, F., Lu, X., Fernandez-Cuesta, L., Bosco, G., et al. (2015). Comprehensive genomic profiles of small cell lung cancer. Nature *524*, 47–53.

Gustafson, W.C., Meyerowitz, J.G., Nekritz, E.A., Chen, J., Benes, C., Charron, E., Simonds, E.F., Seeger, R., Matthay, K.K., Hertz, N.T., et al. (2014). Drugging MYCN through an allosteric transition in Aurora kinase A. Cancer Cell *26*, 414–427.

Hodgkinson, C.L., Morrow, C.J., Li, Y., Metcalf, R.L., Rothwell, D.G., Trapani, F., Polanski, R., Burt, D.J., Simpson, K.L., Morris, K., et al. (2014). Tumorigenicity and genetic profiling of circulating tumor cells in small-cell lung cancer. Nat. Med. *20*, 897–903.

Hook, K.E., Garza, S.J., Lira, M.E., Ching, K.A., Lee, N.V., Cao, J., Yuan, J., Ye, J., Ozeck, M., Shi, S.T., et al. (2012). An integrated genomic approach to identify predictive biomarkers of response to the aurora kinase inhibitor PF-03814735. Mol. Cancer Ther. *11*, 710–719.

Huijbers, I.J., Bin Ali, R., Pritchard, C., Cozijnsen, M., Kwon, M.C., Proost, N., Song, J.Y., de Vries, H., Badhai, J., Sutherland, K., et al. (2014). Rapid target gene validation in complex cancer mouse models using re-derived embryonic stem cells. EMBO Mol. Med. *6*, 212–225.

Jackson, E.L., Willis, N., Mercer, K., Bronson, R.T., Crowley, D., Montoya, R., Jacks, T., and Tuveson, D.A. (2001). Analysis of lung tumor initiation and progression using conditional expression of oncogenic K-ras. Genes Dev. *15*, 3243–3248.

Johnson, B.E., Ihde, D.C., Makuch, R.W., Gazdar, A.F., Carney, D.N., Oie, H., Russell, E., Nau, M.M., and Minna, J.D. (1987). myc family oncogene amplification in tumor cell lines established from small cell lung cancer patients and its relationship to clinical status and course. J. Clin. Invest. *79*, 1629–1634.

Johnson, B.E., Brennan, J.F., Ihde, D.C., and Gazdar, A.F. (1992). myc family DNA amplification in tumors and tumor cell lines from patients with small-cell lung cancer. J. Natl. Cancer Inst. Monogr. *13*, 39–43.

Johnson, B.E., Russell, E., Simmons, A.M., Phelps, R., Steinberg, S.M., Ihde, D.C., and Gazdar, A.F. (1996). MYC family DNA amplification in 126 tumor cell lines from patients with small cell lung cancer. J. Cell Biochem. Suppl. *24*, 210–217.

Kalemkerian, G.P., Akerley, W., Bogner, P., Borghaei, H., Chow, L.Q., Downey, R.J., Gandhi, L., Ganti, A.K., Govindan, R., Grecula, J.C., et al. (2013). Small cell lung cancer. J. Natl. Compr. Canc. Net. *11*, 78–98.

McFadden, D.G., Papagiannakopoulos, T., Taylor-Weiner, A., Stewart, C., Carter, S.L., Cibulskis, K., Bhutkar, A., McKenna, A., Dooley, A., Vernon, A., et al. (2014). Genetic and clonal dissection of murine small cell lung carcinoma progression by genome sequencing. Cell *156*, 1298–1311.

Melichar, B., Adenis, A., Lockhart, A.C., Bennouna, J., Dees, E.C., Kayaleh, O., Obermannova, R., DeMichele, A., Zatloukal, P., Zhang, B., et al. (2015). Safety and activity of alisertib, an investigational aurora kinase A inhibitor, in patients with breast cancer, small-cell lung cancer, non-small-cell lung cancer, head and neck squamous-cell carcinoma, and gastro-oesophageal adenocarcinoma: a five-arm phase 2 study. Lancet Oncol. *16*, 395–405.

Meuwissen, R., Linn, S.C., Linnoila, R.I., Zevenhoven, J., Mooi, W.J., and Berns, A. (2003). Induction of small cell lung cancer by somatic inactivation of both Trp53 and Rb1 in a conditional mouse model. Cancer Cell *4*, 181–189.

Mukhopadhyay, A., Berrett, K.C., Kc, U., Clair, P.M., Pop, S.M., Carr, S.R., Witt, B.L., and Oliver, T.G. (2014). Sox2 cooperates with Lkb1 loss in a mouse model of squamous cell lung cancer. Cell Rep. *8*, 40–49.

Oliver, T.G., Mercer, K.L., Sayles, L.C., Burke, J.R., Mendus, D., Lovejoy, K.S., Cheng, M.H., Subramanian, A., Mu, D., Powers, S., et al. (2010). Chronic cisplatin treatment promotes enhanced damage repair and tumor progression in a mouse model of lung cancer. Genes Dev. *24*, 837–852.

Osborne, J.K., Larsen, J.E., Shields, M.D., Gonzales, J.X., Shames, D.S., Sato, M., Kulkarni, A., Wistuba, I.I., Girard, L., Minna, J.D., and Cobb, M.H. (2013). NeuroD1 regulates survival and migration of neuroendocrine lung carcinomas via signaling molecules TrkB and NCAM. Proc. Natl. Acad. Sci. USA *110*, 6524–6529.

Otto, T., Horn, S., Brockmann, M., Eilers, U., Schuttrumpf, L., Popov, N., Kenney, A.M., Schulte, J.H., Beijersbergen, R., Christiansen, H., et al. (2009). Stabilization of N-Myc is a critical function of Aurora A in human neuroblastoma. Cancer Cell *15*, 67–78.

Peifer, M., Fernandez-Cuesta, L., Sos, M.L., George, J., Seidel, D., Kasper, L.H., Plenker, D., Leenders, F., Sun, R., Zander, T., et al. (2012). Integrative genome analyses identify key somatic driver mutations of small-cell lung cancer. Nat. Genet. *44*, 1104–1110.

Pietanza, M.C., Byers, L.A., Minna, J.D., and Rudin, C.M. (2015). Small cell lung cancer: will recent progress lead to improved outcomes? Clin. Cancer Res. *21*, 2244–2255.

Poirier, J.T., Dobromilskaya, I., Moriarty, W.F., Peacock, C.D., Hann, C.L., and Rudin, C.M. (2013). Selective tropism of Seneca Valley virus for variant subtype small cell lung cancer. J. Natl. Cancer Inst. *105*, 1059–1065.

Poirier, J.T., Gardner, E.E., Connis, N., Moreira, A.L., de Stanchina, E., Hann, C.L., and Rudin, C.M. (2015). DNA methylation in small cell lung cancer defines distinct disease subtypes and correlates with high expression of EZH2. Oncogene *34*, 5869–5878.

Polley, E., Kunkel, M., Evans, D., Silvers, T., Delosh, R., Laudeman, J., Ogle, C., Reinhart, R., Selby, M., Connelly, J., et al. (2016). Small cell lung cancer screen of oncology drugs, investigational agents, and gene and microRNA expression. J. Natl. Cancer Inst. *108*, http://dx.doi.org/10.1093/jnci/djw122.

Rekhtman, N. (2010). Neuroendocrine tumors of the lung: an update. Arch. Pathol. Lab. Med. *134*, 1628–1638.

Rudin, C.M., Durinck, S., Stawiski, E.W., Poirier, J.T., Modrusan, Z., Shames, D.S., Bergbower, E.A., Guan, Y., Shin, J., Guillory, J., et al. (2012). Comprehensive genomic analysis identifies SOX2 as a frequently amplified gene in small-cell lung cancer. Nat. Genet. *44*, 1111–1116.

Sage, J., Miller, A.L., Perez-Mancera, P.A., Wysocki, J.M., and Jacks, T. (2003). Acute mutation of retinoblastoma gene function is sufficient for cell cycle re-entry. Nature *424*, 223–228.

Saunders, L.R., Bankovich, A.J., Anderson, W.C., Aujay, M.A., Bheddah, S., Black, K., Desai, R., Escarpe, P.A., Hampl, J., Laysang, A., et al. (2015). A DLL3-targeted antibody-drug conjugate eradicates high-grade pulmonary neuroendocrine tumor-initiating cells in vivo. Sci. Transl. Med. *7*, 302ra136.

Schaffer, B.E., Park, K.S., Yiu, G., Conklin, J.F., Lin, C., Burkhart, D.L., Karnezis, A.N., Sweet-Cordero, E.A., and Sage, J. (2010). Loss of p130 accelerates tumor development in a mouse model for human small-cell lung carcinoma. Cancer Res. *70*, 3877–3883.

Schoffski, P., Besse, B., Gauler, T., de Jonge, M.J., Scambia, G., Santoro, A., Davite, C., Jannuzzo, M.G., Petroccione, A., and Delord, J.P. (2015). Efficacy and safety of biweekly i.v. administrations of the Aurora kinase inhibitor danusertib hydrochloride in independent cohorts of patients with advanced or metastatic breast, ovarian, colorectal, pancreatic, small-cell and non-small-cell lung cancer: a multi-tumour, multi-institutional phase II study. Ann. Oncol. *26*, 598–607.

Semenova, E.A., Nagel, R., and Berns, A. (2015). Origins, genetic landscape, and emerging therapies of small cell lung cancer. Genes Dev. *29*, 1447–1462.

Semenova, E.A., Kwon, M.C., Monkhorst, K., Song, J.Y., Bhaskaran, R., Krijgsman, O., Kuilman, T., Peters, D., Buikhuisen, W.A., Smit, E.F., et al. (2016). Transcription factor NFIB is a driver of small cell lung cancer progression in mice and marks metastatic disease in patients. Cell Rep. *16*, 631–643.

Sos, M.L., Dietlein, F., Peifer, M., Schottle, J., Balke-Want, H., Muller, C., Koker, M., Richters, A., Heynck, S., Malchers, F., et al. (2012). A framework for identification of actionable cancer genome dependencies in small cell lung cancer. Proc. Natl. Acad. Sci. USA *109*, 17034–17039.

Sutherland, K.D., Proost, N., Brouns, I., Adriaensen, D., Song, J.Y., and Berns, A. (2011). Cell of origin of small cell lung cancer: inactivation of Trp53 and Rb1 in distinct cell types of adult mouse lung. Cancer Cell *19*, 754–764.

Toyoshima, M., Howie, H.L., Imakura, M., Walsh, R.M., Annis, J.E., Chang, A.N., Frazier, J., Chau, B.N., Loboda, A., Linsley, P.S., et al. (2012). Functional genomics identifies therapeutic targets for MYC-driven cancer. Proc. Natl. Acad. Sci. USA *109*, 9545–9550.

Travis, W.D. (2009). Lung tumours with neuroendocrine differentiation. Eur. J. Cancer *45* (*Suppl 1*), 251–266.

Travis, W.D. (2012). Update on small cell carcinoma and its differentiation from squamous cell carcinoma and other non-small cell carcinomas. Mod. Pathol. *25* (*Suppl 1*), S18–S30.

Travis, W.D., Brambilla, E., Nicholson, A.G., Yatabe, Y., Austin, J.H., Beasley, M.B., Chirieac, L.R., Dacic, S., Duhig, E., Flieder, D.B., et al. (2015). The 2015 World Health Organization classification of lung tumors: impact of genetic, clinical and radiologic advances since the 2004 classification. J. Thorac. Oncol. *10*, 1243–1260.

Wilkinson, R.W., Odedra, R., Heaton, S.P., Wedge, S.R., Keen, N.J., Crafter, C., Foster, J.R., Brady, M.C., Bigley, A., Brown, E., et al. (2007). AZD1152, a selective inhibitor of Aurora B kinase, inhibits human tumor xenograft growth by inducing apoptosis. Clin. Cancer Res. *13*, 3682–3688.

Yang, D., Liu, H., Goga, A., Kim, S., Yuneva, M., and Bishop, J.M. (2010). Therapeutic potential of a synthetic lethal interaction between the MYC proto-oncogene and inhibition of aurora-B kinase. Proc. Natl. Acad. Sci. USA *107*, 13836–13841.